Acta Pharmaceutica Sinica B 2023;13(1):213–226

Chinese Pharmaceutical Association
Institute of Materia Medica, Chinese Academy of Medical Sciences

Acta Pharmaceutica Sinica B

www.elsevier.com/locate/apsb
www.sciencedirect.com

ORIGINAL ARTICLE

Structure–activity relationship of pyrazol-4-yl-pyridine derivatives and identification of a radiofluorinated probe for imaging the muscarinic acetylcholine receptor M_4

Ahmed Haider[a,†], Xiaoyun Deng[a,b,†], Olivia Mastromihalis[c,†], Stefanie K. Pfister[a], Troels E. Jeppesen[a], Zhiwei Xiao[a], Vi Pham[c,d], Shaofa Sun[e], Jian Rong[a], Chunyu Zhao[a], Jiahui Chen[a], Yinlong Li[a], Theresa R. Connors[f], April T. Davenport[g], James B. Daunais[g], Vahid Hosseini[h], Wenqing Ran[i], Arthur Christopoulos[c,d], Lu Wang[i], Celine Valant[c,d,*], Steven H. Liang[a,*]

[a]*Department of Radiology, Division of Nuclear Medicine and Molecular Imaging Massachusetts General Hospital and Harvard Medical School, Boston, MA 02114, USA*
[b]*Department of Nuclear Medicine, Tongji Hospital, Tongji Medical College, Huazhong University of Science and Technology, Wuhan 430030, China*
[c]*Drug Discovery Biology, Monash Institute of Pharmaceutical Sciences, Monash University, Parkville, VIC 3052, Australia*
[d]*Neuromedicines Discovery Centre, Monash Institute of Pharmaceutical Sciences, Monash University, Parkville, VIC 3052, Australia*
[e]*Hubei Collaborative Innovation Centre for Non-power Nuclear Technology, College of Nuclear Technology & Chemistry and Biology, Hubei University of Science and Technology, Xianning 437100, China*
[f]*Department of Neurology, Massachusetts General Hospital, Harvard Medical School, Boston, MA 02114, USA*
[g]*Department of Physiology and Pharmacology, Wake Forest School of Medicine, Winston Salem, NC 27157, USA*
[h]*Terasaki Institute for Biomedical Innovation (TIBI), Los Angeles, CA 90024, USA*
[i]*Center of Cyclotron and PET Radiopharmaceuticals, Department of Nuclear Medicine and PET/CT-MRI Center, the First Affiliated Hospital of Jinan University, Guangzhou 510630, China*

Received 22 January 2022; received in revised form 13 May 2022; accepted 22 June 2022

*Corresponding authors. Tel./fax.: +1 617 230 5491.
E-mail addresses: celine.valant@monash.edu (Celine Valant), liang.steven@mgh.harvard.edu, hceline.valant@monash.edu (Steven H. Liang).
[†]These authors made equal contributions to this work.
Peer review under the responsibility of Chinese Pharmaceutical Association and Institute of Materia Medica, Chinese Academy of Medical Sciences.

https://doi.org/10.1016/j.apsb.2022.07.008

KEY WORDS

Muscarinic acetylcholine receptor;
Positron emission tomography;
Neuroimaging;
Neuropharmacology;
Neurological disorders

Abstract There is an accumulating body of evidence implicating the muscarinic acetylcholine receptor 4 (M_4) in schizophrenia and dementia with Lewy bodies, however, a clinically validated M_4 positron emission tomography (PET) radioligand is currently lacking. As such, the aim of this study was to develop a suitable M_4 PET ligand that allows the non-invasive visualization of M_4 in the brain. Structure−activity relationship studies of pyrazol-4-yl-pyridine derivates led to the discovery of target compound **12** — a subtype-selective positive allosteric modulator (PAM). The radiofluorinated analogue, [^{18}F]**12**, was synthesized in 28 ± 10% radiochemical yield, >37 GBq/μmol and an excellent radiochemical purity >99%. Initial *in vitro* autoradiograms on rodent brain sections were performed in the absence of carbachol and showed moderate specificity as well as a low selectivity of [^{18}F]**12** for the M_4-rich striatum. However, in the presence of carbachol, a significant increase in tracer binding was observed in the rat striatum, which was reduced by >60% under blocking conditions, thus indicating that orthosteric ligand interaction is required for efficient binding of [^{18}F]**12** to the allosteric site. Remarkably, however, the presence of carbachol was not required for high specific binding in the non-human primate (NHP) and human striatum, and did not further improve the specificity and selectivity of [^{18}F]**12** in higher species. These results pointed towards significant species-differences and paved the way for a preliminary PET study in NHP, where peak brain uptake of [^{18}F]**12** was found in the putamen and temporal cortex. In conclusion, we report on the identification and preclinical development of the first radiofluorinated M_4 PET radioligand with promising attributes. The availability of a clinically validated M_4 PET radioligand harbors potential to facilitate drug development and provide a useful diagnostic tool for non-invasive imaging.

1. Introduction

Muscarinic acetylcholine receptors (mAChRs) belong to the superfamily of G-protein-coupled receptors (GPCRs) and mediate signal transduction of the endogenous neurotransmitter acetylcholine (ACh) in both the central and peripheral mammalian nervous system[1−3]. To date, five distinct mAChR subtypes, denoted M_1 to M_5, have been described[4]. While M_1, M_3 and M_5 predominantly couple to GPCR's *via* the G_q protein alpha subunit ($G_{q/11}$), M_2 and M_4 preferentially facilitate signal transduction though the G_i and G_o protein alpha subunits ($G_{i/o}$)[5]. Accordingly, the activation of M_2 and M_4 by ACh globally leads to an inhibition of adenylyl cyclase, followed by reduction of cyclic AMP (cAMP) formation[6,7]. Owing to the broad implications of M_4 receptors in central nervous system (CNS)-related pathologies, including Alzheimer's disease (AD)[8,9], schizophrenia[10,11] and dementia with Lewy bodies (DLB)[12], M_4 activation *via* synthetic agonists has proven to be of high therapeutic value. Further, potential links between M_4 receptors and behavioral disorders such as alcohol use disorder[13] and cocaine self-administration have been recently observed in rodents[14].

Previous studies revealed that muscarinic M_4 receptors are markedly expressed in the mammalian brain, with high abundancies in the striatum, thalamus and cortex[15−18]. Notably, considerable species differences have been described for the localization and structure of M_4[7,19−21], explaining the variability of binding affinities for some synthetic M_4 ligands across different species[22,24]. Strenuous drug development efforts prompted the discovery of several M_4 agonists, however, due to the high degree of structural homology among the orthosteric site of the different mAChR subtypes, the identification of an orthosteric M_4-selective ligand has proven challenging[23−26]. An important breakthrough in M_4-targeted drug development was achieved with the discovery of the first generation of selective PAMs that included LY2033298 and VU010010[27−29]. These PAMs elicit pharmacological activity by enhancing the binding affinity or functional activity of ACh towards M_4[27,28]. Notwithstanding the high affinity and selectivity of VU010010 for M_4 receptors, its further development was plagued by solubility issues and P-glycoprotein (P-gp) efflux *in vivo*[29]. Other derivatives of the same series include, but are not limited to, VU0152099 and VU0152100 (ML108)[30−33], VU0467154[34,35], VU0409524 (ML293)[36], VU6000918[37], VU0448088[38], VU6028418[39] as well as VU0467485 (AZ13713945)[40] (Fig. 1), but clinical trials with these compounds have not been reported to date. Indeed, M_4-selective targeted therapy is far from routine clinical use and the majority of reported ligands were plagued by inappropriate bioavailability and CNS exposure, high P-gp efflux liability, species variability, and poor metabolic stability or selectivity for M_4. This has, at least in part, been attributed to the lack of appropriate tools for target engagement studies *in vivo*.

Positron emission tomography (PET) is a powerful non-invasive imaging modality that allows real-time quantification of biochemical processes. As such, the availability of an appropriate M_4 PET ligand can facilitate the development of M_4-targeted compounds *via* receptor occupancy assessment in living subjects. While numerous therapeutic ligands have been reported, the development of M_4 PET radioligands is lagging behind. We recently reported on the synthesis and biological evaluation of [^{11}C]VU0467485, as well as two other carbon-11 labeled derivatives bearing an additional fluorine atom at different positions of the phenyl moiety[41]. Despite obtaining some degree of specific binding by *in vitro* autoradiography, this class of compounds was deemed unsuitable for *in vivo* applications due to low brain uptake[41]. Similarly, radiofluorination of the 1,3-dihydro-pyrrolopyridine, M_4R-1911, yielded a PET radioligand with poor blood−brain barrier (BBB) penetration[42]. Recently, Tong et al.[43] disclosed the preclinical evaluation of the first promising M_4-targeted probe, codenamed [^{11}C]MK-6884, that was based on a

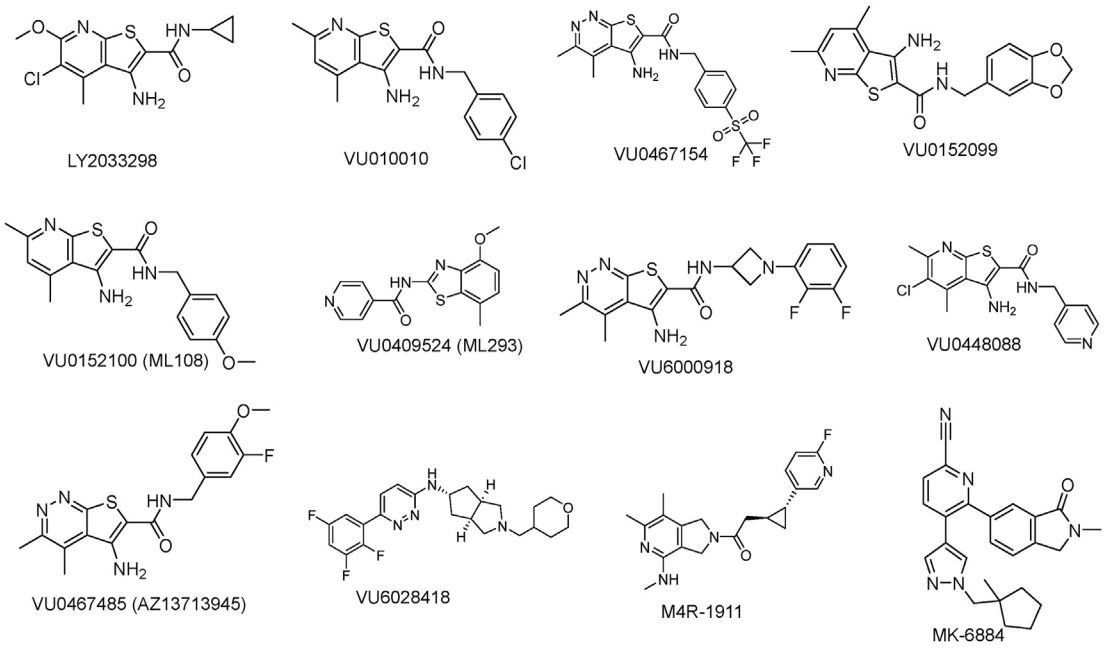

Figure 1 Selected muscarinic acetylcholine receptor subtype 4 (M_4) ligands.

pyrazol-4-yl-pyridine core structure and exhibited good brain uptake and M_4-specific signal in rhesus monkey PET. Nonetheless, the relatively short physical half-life of [^{11}C]MK-6884 confines its use to nuclear medicine facilities with an on-site cyclotron and the availability of a suitable radiofluorinated analogue with improved image quality as well as longer physical half-life is warranted.

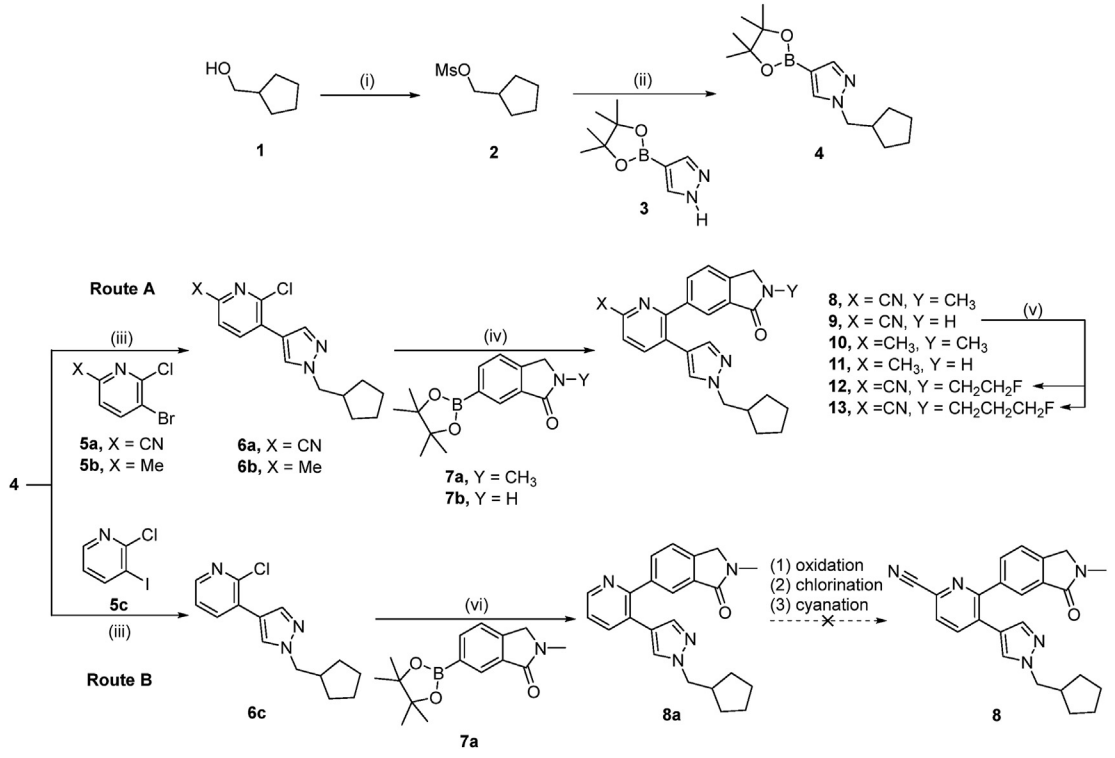

Scheme 1 Reagents and conditions: (i) 2 equiv. MsCl, 4.4 equiv. Et_3N, EtOAc, 0 °C to room temperature, 30 min, 95%; (ii) 1.5 equiv. **3**, 1.8 equiv. NaH (60%), DMF, room temperature to 60 °C, 3 h, 75%; (iii) 1.2 equiv. **5a**, **5b** or **5c**, 20% (mol/mol) Pd(dppf)Cl_2, 2.5 equiv. K_2CO_3, 1,4-dioxane/H_2O (3/1), room temperature, 10 min, 100 °C, 3 h, 53% for **6a**, 65% for **6b**, 41% for **6c**; (iv) 1.2 equiv. **7a** or **7b**, 20% (mol/mol) Pd(dtbpf)Cl_2, 3 equiv. K_2CO_3, 1,4-dioxane/H_2O (3/1), room temperature, 10 min, 100 °C, 3 h, 64% for **8**, 66% for **9**, 53% for **10**, 26% for **11**; (v) 1.7 equiv. NaH, THF, room temperature to 60 °C, 4 h, 2 equiv. ICH_2CH_2F for **12**, 39%, 2 equiv. $ICH_2CH_2CH_2F$ for **13**, 37%; (vi) 1.2 equiv. **7a**, 20% (mol/mol) Pd(dtbpf)Cl_2, 3 equiv. K_2CO_3, THF/H_2O (3/2), room temperature, 10 min, 60 °C, 5 h, 28%. DMF, *N*,*N*-dimethylformamide; dppf, 1,1′-bis(diphenylphosphino)ferrocene; dtbpf, 1,1′-bis(di-*tert*-butylphosphino)ferrocene; THF, tetrahydrofuran.

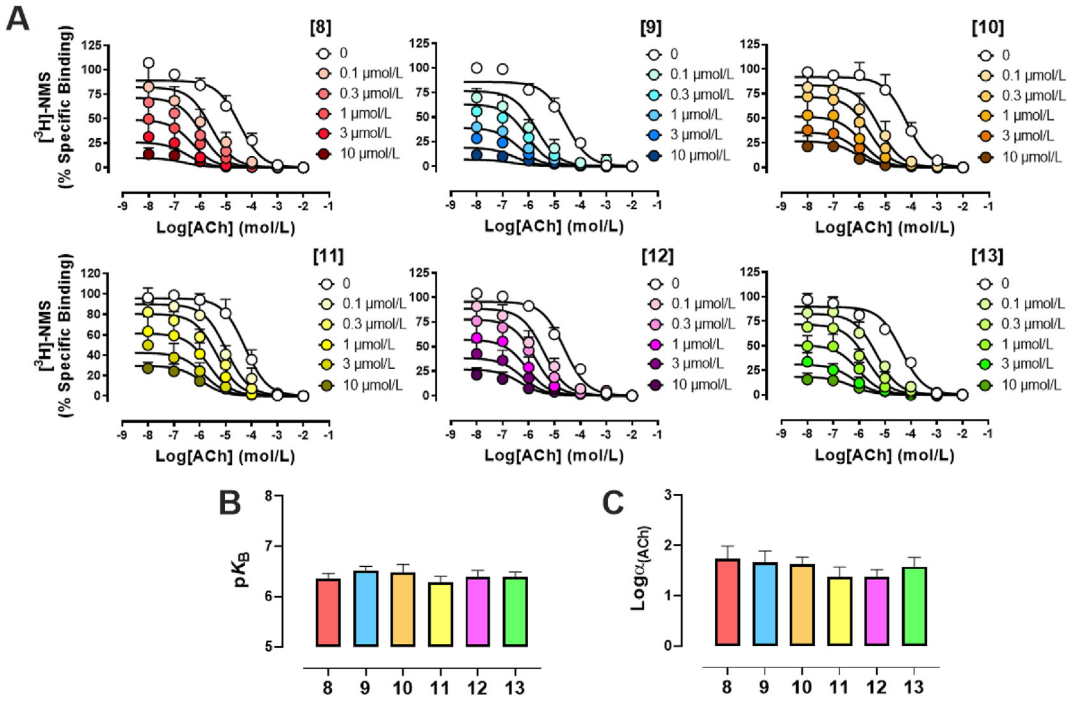

Figure 2 Allosteric binding properties of pyrazol-4-yl-pyridine compounds **8**−**13** at the hM_4 mAChR. (A) Radioligand binding experiments using CHO cells stably expressing the hM_4 in the presence of a K_D concentration of the radiolabeled antagonist [^{3}H]NMS (~0.1 nmol/L, increasing concentrations of ACh with or without increasing concentrations of **8**−**13**. (B) Affinity parameters and (C) cooperativity parameters of pyrazol-4-yl-pyridine compounds obtained using the ATCM [Eq. (1)]. Values represent the mean ± SEM obtained from three experiments conducted in duplicate (total $n = 6$).

Here, we present the synthesis and pharmacological evaluation of a new series of pyrazol-4-yl-pyridine-based M_4-selective ligands, of which a radiofluorinated probe was developed that allows satellite distribution and broadens the scope of PET-guided ligand development in the field[44].

2. Results and discussion

2.1. Chemistry

Based on a set of previously reported pyrazol-4-yl-pyridines, that exhibited potential as positive allosteric modulators of M_4 muscarinic acetylcholine receptors[45], we designed a focused library of small molecules that were amenable for carbon-11 or fluorine-18 labeling. Initial attempts to introduce a cyano moiety at the final step to allow structural modification at the pyridine ring *via* route B failed to afford the desired target compound **8** (Scheme 1). Along this line, we envisioned to synthesize target compound **8** *via* route A. Given that route A readily afforded target compound **8**, this route was deemed more suitable for the synthesis of target compounds **9**−**13**. As depicted in Scheme 1 (route A), a mesylate leaving group was installed to alcohol **1** by reacting it with MsCl in the presence of Et_3N, affording cyclopentylmethyl methanesulfonate **2** in 95% chemical yield. Subsequent *N*-alkylation of pyrazole boronic ester with compound **2** gave boronic ester **4** in 75% yield. Stepwise Suzuki coupling reactions afforded pyrazol-4-yl-pyridines **8**−**11**. In particular, the palladium catalyzed cross coupling between bromide **5a** or **5b** and boronic acid ester **4** led to the formation of compounds **6a** and **6b** in 53% or 65% yield, respectively. Similarly, palladium catalyzed cross coupling reaction of **6a** and **6b** with boronic acid ester **7a** or **7b**, respectively, afforded target compounds **8**−**11** in chemical yields ranging from 26% to 66%.

It is worth mentioning that the electron-withdrawing cyano moiety of pyridine **5a**, as compared to the methyl substituent in pyridine **5b**, led to an improved oxidative addition with palladium catalyst during coupling reactions, thus providing superior overall yields for the synthesis of target compounds **8** and **9**, as compared to **10** and **11**. Notably, pyrazol-4-yl-pyridine derivatives **9** and **11** were prepared in reasonable yields without protection of the N−H moiety. As for the fluorinated analogs, *N*-alkylation of amide **9** gave fluoroethyl derivative **12** and fluoropropyl analog **13**, respectively. In summary, target compounds **8**−**13** were obtained *via* route A (Scheme 1) from commercially available cyclopentylmethanol in 4−5 steps with overall yields of 7%−18%.

2.2. Pharmacology

Novel pyrazol-4-yl-pyridine compounds were first investigated in radioligand binding against [^{3}H]NMS at the human M_4, in order to quantify the affinity of these compounds for the allosteric site, pK_B, and their binding cooperativity with the endogenous ligand ACh, $\log\alpha_{ACh}$, as an indication of strength and direction of modulation with the natural hormone for the receptor (Fig. 2A). As expected, increasing concentrations of analogues **8**−**13** induced a strong leftward shift of the affinity binding inhibition curve of ACh at the M_4, validating all pyrazol-4-yl-pyridine compounds as PAMs. Using an allosteric ternary complex model to analyze the data [Eq. (1)], we estimated pK_B values ranging between 6.3 and 6.5, and that PAM binding is able to induce ~25−50-fold increase in the affinity of ACh for the orthosteric

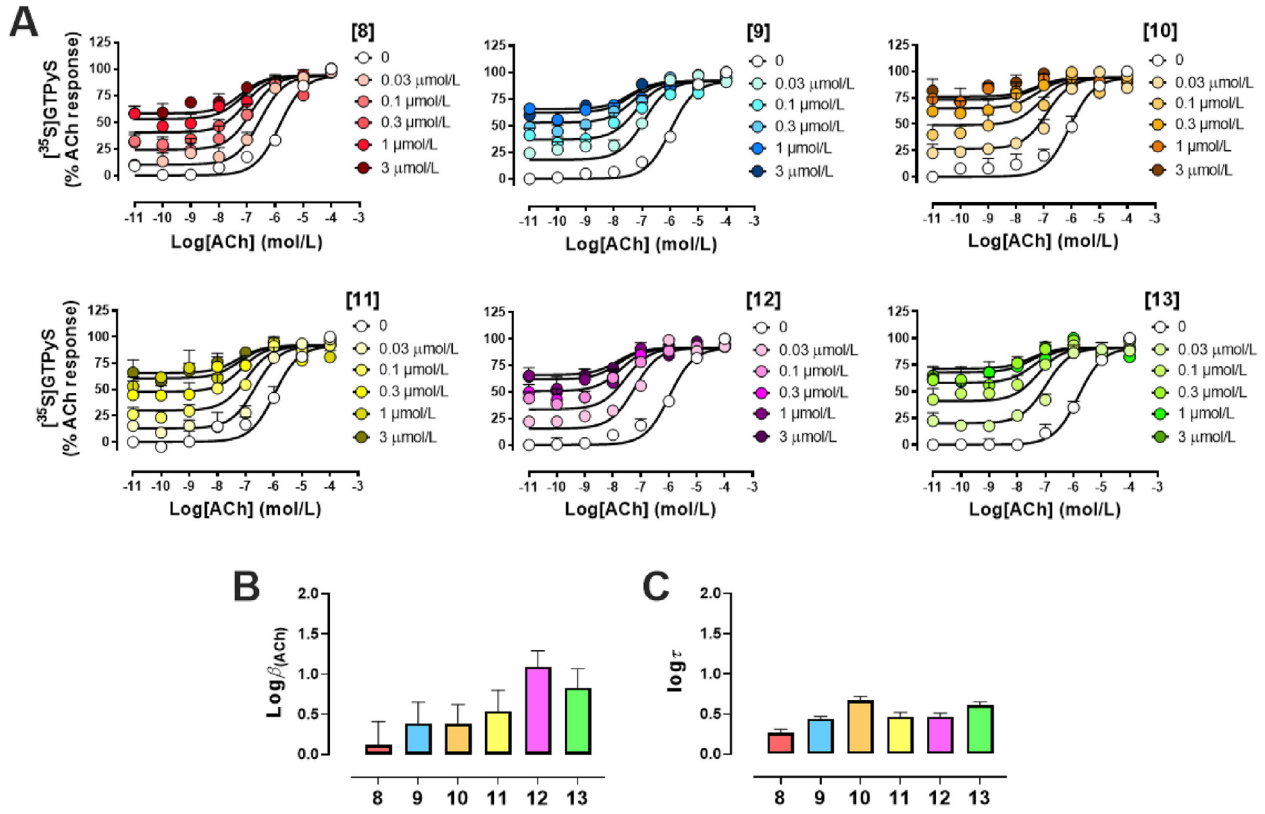

Figure 3 Allosteric functional properties of pyrazol-4-yl-pyridine **8**−**13** at the hM_4. (A) ACh-mediated [^{35}S]-GTPγS accumulation binding curves in absence or presence of increasing concentrations of pyrazol-4-yl-pyridine compounds. (B) Efficacy cooperativity parameters and (C) efficacy parameters of pyrazol-4-yl-pyridine compounds obtained using the operational model of allosterism [Eq. (2)]. Values represent the mean ± SEM obtained from three experiments conducted in duplicate (total $n = 6$).

site, $\log\alpha_{ACh} = 1.38-1.74$ (Fig. 2B and C). Compared against each other, the binding affinity and binding cooperativity with ACh, of pyrazol-4-yl-pyridine compounds **8**−**13** were not statistically significant from each other, suggesting that the subtle chemical modifications around the core of the M_4 PAMs were neither affecting the ability of each compound to recognize and interact with the allosteric site of the M_4, nor influencing their allosteric transmission properties. Interestingly, all pyrazol-4-yl-pyridine compounds displayed strong negative binding allosteric properties with the radiolabeled antagonist [^{3}H]NMS, as seen by a dramatic depression in the [^{3}H]NMS specific binding with increasing concentrations of M_4-PAMs. This is undoubtedly consistent with the fact that **8**−**13** stabilize a conformation of M_4 that is favorable for agonists to bind and therefore, less preferable for an antagonist such as *N*-methylscopolamine, inherently reducing its binding capability. In order to assess the mode of action of pyrazol-4-yl-pyridines **8**−**13** at a signaling level, we decided to investigate their allosteric properties in a functional assay, proximal to $G_{i/o}$ coupled receptor interaction, using the [^{35}S]-GTPγS accumulation binding assay.

As anticipated, all six analogues were able, in a concentration dependent manner, to promote a strong leftward shift of the ACh-mediated concentration-response curve (Fig. 3A), consistent with the PAM effect observed in radioligand binding (Fig. 2A). In

Table 1 Pharmacological parameters of pyrazol-4-yl-pyridine **8**−**13** at the hM_4. Values represent the mean ± SEM obtained from three experiments conducted in duplicate.

Parameters	8	9	10	11	12	13
pK_B[a]	6.4 ± 0.1	6.5 ± 0.1	6.5 ± 0.2	6.3 ± 0.1	6.4 ± 0.1	6.4 ± 0.1
$\log\alpha_{ACh}$[b]	1.7 ± 0.3	1.7 ± 0.2	1.6 ± 0.2	1.4 ± 0.2	1.4 ± 0.1	1.6 ± 0.2
$\log\alpha\beta_{ACh}$[c]	1.9 ± 0.2	2.0 ± 0.1	2.0 ± 0.2	1.9 ± 0.2	2.5 ± 0.1[f]	2.4 ± 0.2[f]
$\log\beta_{ACh}$[d]	0.1 ± 0.3	0.4 ± 0.3	0.4 ± 0.2	0.5 ± 0.3	1.1 ± 0.2	0.8 ± 0.2
$\log\tau$[e]	0.3 ± 0.0	0.4 ± 0.0	0.7 ± 0.0	0.5 ± 0.0	0.5 ± 0.0	0.6 ± 0.0

[a]Negative logarithm of the equilibrium dissociation constant of M_4-PAMs.
[b]Logarithm of the binding (α) cooperativity factor between M_4-PAMs and ACh.
[c]Logarithm of the operational functional ($\alpha\beta$) cooperativity factors between ACh and M_4-PAMs.
[d]Logarithm of the activation (β) cooperativity factors between ACh and M_4-PAMs, determined by subtracting (α) from the ($\alpha\beta$) parameters.
[e]Logarithm of the operational efficacy parameter of M_4-PAMs as allosteric agonists.
[f]Significantly different ($P < 0.05$) from $\log\alpha_{ACh}$ values as determined by a multiple unpaired *t*-test.

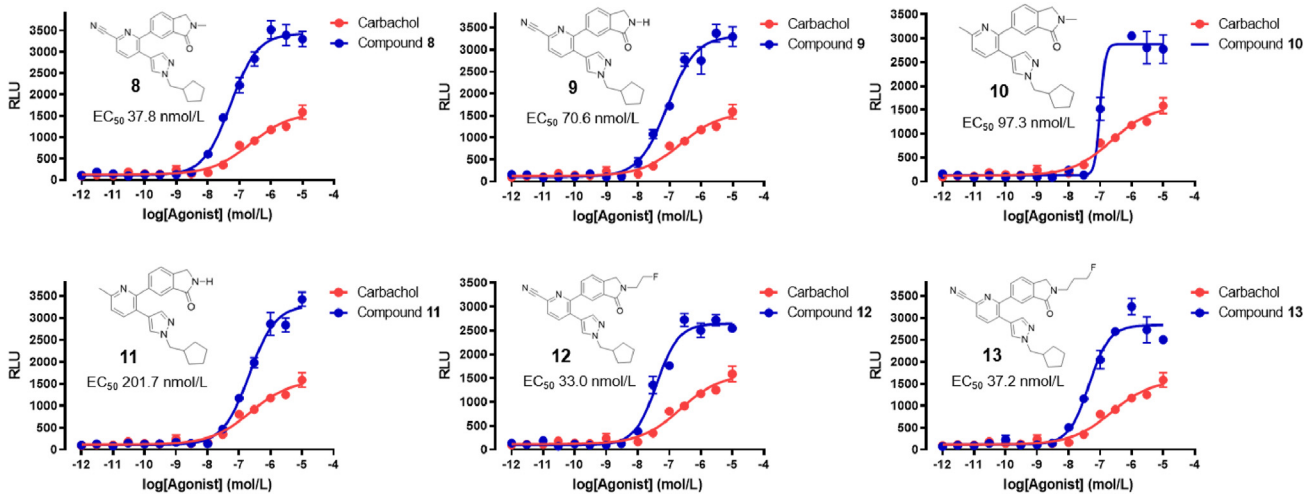

Figure 4 Acetylcholine receptor M_4 Tango assay for target compounds **8**–**13**.

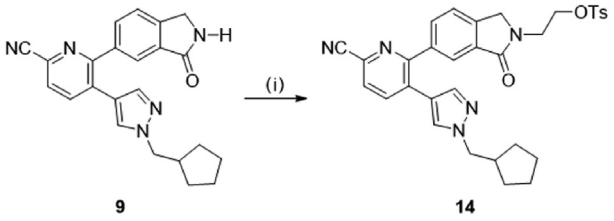

Scheme 2 Synthesis of tosylate precursor **14** for radiofluorination. (i) 1.2 equiv. NaH, 2 equiv. $TsOCH_2CH_2OTs$, DMF, room temperature to 60 °C, 2 h, 40%.

addition to the leftward shift, we also noted a significant increase in the baseline activity, validating **8**–**13** as ago-PAMs, meaning these pyrazol-4-yl-pyridine compounds can directly activate the M_4 from the allosteric site. Using an operational model of allosterism to fit the data [Eq. (2)], we were able to quantify the functional cooperativity of **8**–**13** with ACh, $\log_{ACh}$, and the degree of agonism, $\log\tau$ (Table 1). Whilst the novel M_4-PAMs displayed similar efficacy in mediating [^{35}S]GTPγS accumulation binding (Fig. 3C), differences in their ability to modulate the efficacy of ACh were observed. In particular, compound **12**, in addition to increasing the binding property of ACh (Fig. 2A), also noticeably increased the endogenous ligand's efficacy, as determined when calculating $\log\beta_{ACh}$ in that pathway (Fig. 3B, Table 1).

We next evaluated target compounds **8**–**13** in a functional Tango assay and compared their ability to induce signal transduction *via* protease-tagged β-arrestin recruitment to that of the commercially available M_4 agonist, carbachol (Fig. 4). In concert with the radioligand binding assays, we observed that all target compounds exhibited considerable M_4 activity, with EC_{50} values ranging from 33 to 202 nmol/L. While target compounds **8**–**13** were more potent than carbachol, we observed that compounds carrying a cyano moiety at the pyridine core generally exhibited an improved potency, as compared to their methylated analogues. Similarly, substitution of the hydrogen atom of the lactam functionality by a methyl group or a fluoroalkyl chain slightly improved potency. Notably, compound **12** showed the highest potency towards M_4 in the Tango assay and was selective over

Table 2 Optimization of reaction conditions for the synthesis of [^{18}F]**12**.

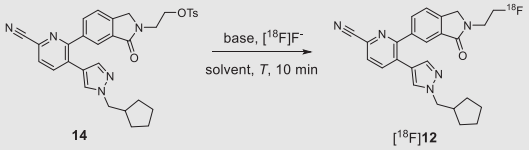

Entry	Solvent[a]	*T* (°C)	Subst. (mg)	Base (mg)	RCC (%)[b]
1	CH_3CN	120	2	K_2CO_3/K_{222} (2/10)	1 ± 0 (n = 2)
2	DMF	120	2	K_2CO_3/K_{222} (2/10)	12 ± 2 (n = 2)
3	DMF	120	2	TEAB (2)	7 ± 3 (n = 2)
4	DMF	120	2	$KHCO_3/K_{222}$ (2/10)	3 ± 3 (n = 2)
5	DMF	120	2	TBAOMs (2)	11 ± 1 (n = 2)
6	^{t}BuOH/MeCN	100	2	TBAOMs (3)	80 ± 16 (n = 2)
7	**^{t}BuOH/MeCN**	**100**	**3**	**TBAOMs (3)**	**91 ± 1 (n = 2)**
8	^{t}BuOH/MeCN	80	3	TBAOMs (3)	59 ± 8 (n = 2)
9	^{t}BuOH/MeCN	120	3	TBAOMs (3)	77 ± 1 (n = 2)

[a]0.4 mL, ^{t}BuOH/MeCN = 0.35/0.05 for entries 6–9.

[b]Incorporation yield and product identity were determined by radio-TLC and radio-HPLC, respectively. The optimal conditions (entry 7) are indicated in bold.

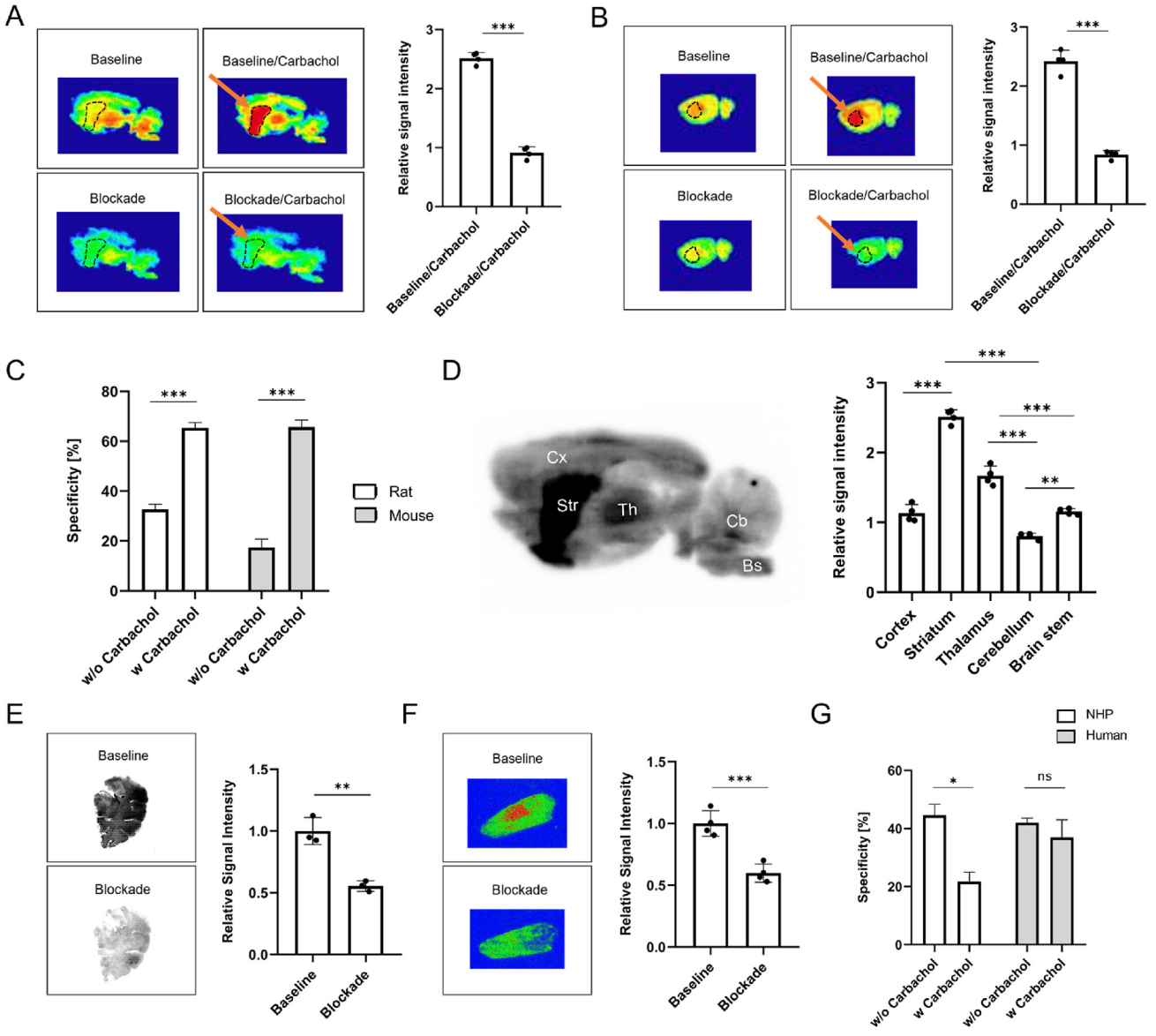

Figure 5 *In vitro* autoradiography of [^{18}F]**12** on rodent, non-human primate (NHP) and human brain tissue sections. (A) Representative autoradiograms of the rat brain in the presence and absence of orthosteric agonist, carbachol. Blocking was performed using an excess of non-radioactive compound **11** (10 µmol/L). Striatal regions were delineated and highlighted with an arrow. Quantification of the radioactive signal is presented for the striatum and in the presence of carbachol. (B) Representative autoradiograms of the mouse brain in the presence and absence of orthosteric agonist, carbachol. Blocking was performed using an excess of non-radioactive compound **11** (10 µmol/L). Striatal regions were delineated and highlighted with an arrow. Quantification of the radioactive signal is presented for the striatum and in the presence of carbachol. (C) Comparison of specificity values for rodents in the presence and absence of carbachol. (D) Regional binding pattern in the rat brain. (E) Representative autoradiograms of the NHP brain and quantification of the radioactive signal. Blocking was performed using an excess of non-radioactive compound **11** (10 µmol/L). (F) Representative autoradiograms of the human putamen and quantification of the radioactive signal. Blocking was performed using an excess of non-radioactive compound **11** (10 µmol/L). (G) Comparison of specificity values for primates in the presence and absence of carbachol.

other muscarinic acetylcholine receptor subtypes, including M_1, M_2, M_3 and M_5 (Supporting Information). Based on the overall pharmacology data, tri-substituted pyridine **12** was deemed most suitable for biological evaluation as a PET radioligand. While the structure of the previously reported carbon-11 labeled analog, [^{11}C]MK-6884, proved suitable for *in vivo* imaging, introduction of a fluorine-bearing side chain led to an increase of lipophilicity. As such, we used a less lipophilic pyrazole substituent to reverse the anticipated increase in lipophilicity induced by the fluoroalkyl side chain, with the aim improve *in vivo* brain uptake.

2.3. *Radiochemistry*

Based on the favorable binding affinity and selectivity, target compound **12** was selected for radiofluorination and biological evaluation as an M_4-selective PET radioligand. Accordingly, tosylate precursor **14** for radiofluorination was prepared *via N*-alkylation of lactam **9** with ethylene ditosylate (Scheme 2). Initially, attempts to synthesize [^{18}F]**12** were conducted in MeCN in the presence of K_2CO_3 at 120 °C (Table 1, entry 1). However, these conditions yielded a poor radiochemical conversion (RCC)

of 1%, as confirmed by radio-TLC. When DMF was used instead of MeCN, in combination with other bases such as TEAB, $KHCO_3$ and TBAOMs, marginal improvements in RCC were obtained (Table 2, entries 2−5).

Notably, the addition of *t*BuOH as a co-solvent with MeCN ultimately resulted in a substantial increase in RCC, as evidenced for entries 6−9 in Table 2.

Further optimization revealed that an amount of 3 mg precursor, alongside a reaction temperature of 100 °C constituted the optimal condition for the radiofluorination of precursor **14**, yielding an RCC of 91% (Table 1, entry 7). Overall, precursor **14** (3 mg) was reacted with [^{18}F]fluoride in the presence of TBAOMs (3 mg) at 100 °C for 10 min to yield [^{18}F]**12** in an average of 28 ± 10% decay-corrected RCY based on starting [^{18}F]fluoride at the end-of-synthesis (60 min synthesis time) with >99% radiochemical purity (n = 3). The molar activity was greater than 1 Ci/μmol (37 GBq/μmol).

2.4. *In vitro autoradiography*

Initial *in vitro* autoradiography studies were conducted with rodent brain tissue sections. Of note, previous reports have shown that agonist binding to the orthosteric binding site of mAChRs can affect the binding properties of the respective PAMs—an observation that was termed probe dependence[26]. Accordingly, we conducted autoradiographic experiments in the presence and in the absence of the commercially available orthosteric M_4 agonist, carbachol. [^{18}F]**12** exhibited M_4-specific binding on rodent brain sections, which was significantly enhanced in the presence of carbachol in rodents (Fig. 5A−D). Indeed, the degree of specific binding increased from 32.6% to 65.4% in rats and from 17.4% to 65.7% in mice ($P < 0.001$ for both species, Fig. 5C), respectively, in the presence of carbachol. In concert with reported M_4 expression patterns, binding of [^{18}F]**12** to distinct rat brain regions by *in vitro* autoradiography revealed highest binding in the striatum, followed by the thalamus and cortex, while uptake in the cerebellum was lowest (Fig. 5D). The latter findings indicate a high selectivity of the probe to the brain regions that exhibit high M_4 abundancy. To assess the utility of [^{18}F]**12** in higher species, we conducted *in vitro* autoradiography studies on NHP whole brain tissue and human post-mortem sections of the putamen, in the presence and absence of carbachol. Notably, we found that specificity values > 40% were obtained without carbachol, and that carbachol addition did not further improve tracer binding to NHP and human M_4 receptors (Fig. 5E−G). Interestingly, on NHP autoradiograms, carbachol addition seemed to reduce the degree of tracer specificity, underlining the importance to account for species-differences in M_4-targeted drug and tracer development.

2.5. *PET experiments*

We next performed PET imaging in non-human primates. Following injection of [^{18}F]**12**, PET and MRI images were acquired (Fig. 6). M_4-rich brain regions such as the putamen and temporal cortex were delineated in the PET image, as shown by the arrows in Fig. 6B. Tracer uptake was highest in the putamen and cortical regions, including the temporal and prefrontal cortex. Nonetheless, the overall brain uptake of [^{18}F]**12** was lower than expected and potential underlying causes may constitute tracer efflux by P-gp proteins that are located at the blood−brain barrier, which can be circumvented by co-administration of a P-gp inhibitor. Although the striatum was delineated from the image, it should be noted that the limited general brain uptake and preliminary nature of the non-human primate studies constitute a limitation of the present study. Of note, however, previous reports unveiled that [^{11}C]MK-6884 peak striatal uptake was higher in humans (peak striatal SUV *ca.* 2.5)[46] than in rhesus monkeys (peak striatal SUV *ca.* 1.2)[43], which points towards improved tracer inflow for this class of compounds in the human brain and warrants similar studies with [^{18}F]**12**. Further, initial tracer inflow and peak SUV in rhesus monkeys were comparable between [^{11}C]MK-6884 and [^{18}F]**12**, thus indicating similar blood−brain barrier permeability. Indeed, peak striatal SUVs in rhesus monkeys were on average 1.1 for [^{18}F]**12**, which was comparable to that of [^{11}C]MK-6884 and is in concert with the structural and physicochemical similarities of the two compounds. However, [^{18}F]**12** exhibited a substantially faster washout from the brain, as compared to [^{11}C]MK-6884, indicating a lower dissociation rate constant for

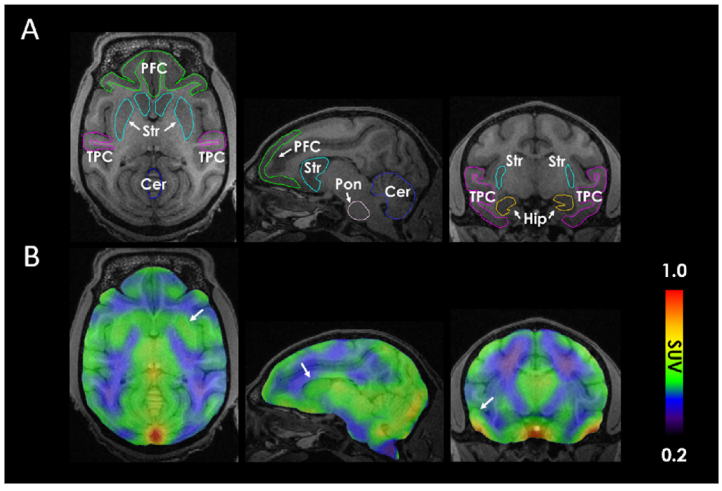

Figure 6 Representative PET/MRI images of the non-human primate (NHP) brain following administration of [^{18}F]**12**. (A) Regional assignment was performed based on the acquired MRI image and an overlay was used to define the regions of interest. (B) Averaged PET images presented in transverse, sagittal and coronal view (left to right). White arrows show the striatum, prefrontal and temporal cortex. Cer, cerebellum; Hip, hippocampus; PFC, prefrontal cortex; Pon, pons; Str, striatum; TPC, temporal cortex.

[^{11}C]MK-6884 towards the allosteric M_4 binding site. It is envisioned that future studies will reveal the extent to which [^{18}F]**12** can be used for M_4-targeted receptor mapping in higher species. Notwithstanding the encouraging findings from cross-species autoradiographic studies, several challenges remain to be addressed in assessing the potential of [^{18}F]**12** for clinical use. First, future studies will aim at establishing the utility of [^{18}F]**12** for *in vivo* target engagement studies, which can be conducted by dose−response studies with validated M_4 ligands. Second, given (1) that previous reports on [^{11}C]MK-6884 showed higher peak striatal uptake in humans than in rhesus monkeys, the question arises whether the structurally similar radiofluorinated probe, [^{18}F]**12**, may as well exhibit a higher brain exposure in humans, as compared to non-human primates. Third, it remains unclear whether [^{18}F]**12** is sensitive to changes in M_4 abundancy under neurodegenerative conditions. While M_4 is heavily implicated in Alzheimer's disease (AD), the development of subtype-selective modulators has proven challenging. The availability of suitable PET probes for non-invasive target engagement studies holds promise to substantially facilitate the development of effective AD therapies.

3. Conclusions

In the past few years, we have witnessed a substantial progress in our understanding of the structure and biology of M_4. Indeed, M_4 has emerged as a valuable target in schizophrenia and dementia with Lewy bodies. While therapeutic ligands have advanced to clinical trials, the development of a suitable probe for non-invasive imaging in humans is lagging behind. In this work, we report on the identification and preclinical development of a radiofluorinated M_4-targeted probe that proved to be specific and selective over the other muscarinic receptor subtypes across different species by *in vitro* autoradiography experiments. Our findings highlighted that species-differences are critical, particularly with regard to the effects of orthostatic M_4 ligand binding on the allosteric binding site. While our probe, [^{18}F]**12**, did not require orthosteric agonist binding in higher species, the interaction of carbachol with M_4 substantially improved the specificity and selectivity of [^{18}F]**12** to the allosteric site in rodents. M_4-rich brain regions such as the putamen and temporal cortex were successfully delineated using PET/MRI in non-human primates, suggesting that the probe is sensitive to the high M_4 expression in those regions. Further studies in healthy NHP and disease models are warranted to assess the utility of [^{18}F]**12** for human application in M_4-related pathologies. A clinically validated M_4 PET radioligand would not only facilitate drug development programs by means of target engagement experiments, but also provide an opportunity for subtype-selective M_4 receptor studies in patients. In the era of precision medicine, innovative diagnostic tools harbor enormous potential to deliver the best possible care for the individual patient.

4. Experimental

All the chemicals employed in the syntheses were purchased from commercial vendors and used without further purification. Thin-layer chromatography (TLC) was conducted with 0.25 mm silica gel plates ($^{60}F_{254}$) and visualized by exposure to UV light (254 nm) or stained with potassium permanganate. Flash column chromatography was performed using silica gel (particle size 0.040−0.063 mm). Nuclear magnetic resonance (NMR) spectra were obtained on a Bruker spectrometer 300 MHz. Chemical shifts (δ) are reported in ppm and coupling constants are reported in Hertz. The multiplicities are abbreviated as follows: s, singlet; d, doublet; t, triplet; q, quartet; quint, quintet; sext, sextet; sept, setpet; m, multiplet; br, broad signal; dd, doublet of doublets. Animal experiments were approved by the Institutional Animal Care and Use Committee of Massachusetts General Hospital. CD1 mice (8 weeks, 20−25 g) were kept on a 12 h light/12 h dark cycle and were allowed food and water *ad libitum*.

4.1. Chemistry

4.1.1. Preparation of cyclopentylmethyl methanesulfonate (2)

MsCl (20 mmol) was added dropwise to a solution of NEt_3 (44 mmol) and **1** (10 mmol) in ethyl acetate (20 mL) at 0 °C. The mixture was stirred at ambient temperature for 30 min. Then H_2O (20 mL) was added and the mixture was extracted with ethyl acetate (2 × 20 mL). The combined organic layers were washed with H_2O (20 mL) brine (20 mL), dried over Na_2SO_4, and concentrated under reduced pressure. The residue could be used in the next steps without extra purification. Compound **2** was prepared in 95% yield as a light-yellow oil. ^{1}H NMR (300 MHz, $CDCl_3$) δ 4.08 (d, J = 7.1 Hz, 2H), 2.98 (s, 3H), 2.41−2.17 (m, 2H), 1.85−1.70 (m, 2H), 1.64−1.51 (m, 2H), 1.35−1.18 (m, 2H).

4.1.2. Preparation of 1-(cyclopentylmethyl)-4-(4,4,5,5-tetramethyl-1,3,2-dioxaborolan-2-yl)-1H-pyrazole (4)

A solution of **3** (9 mmol) in DMF (5 mL) was added dropwise to a solution of NaH (10.8 mmol, 60% suspension) in DMF (5 mL) at 0 °C. The mixture was stirred at ambient temperature for 30 min. A solution of **2** in DMF (5 mL) was added dropwise to the mixture and stirred at 60 °C for 3 h. The reaction was cooled to ambient temperature and quenched with H_2O (15 mL) on an ice bath. The mixture was extracted with ethyl acetate (20 mL × 2). The combined organic layers were washed with H_2O (2 × 20 mL), brine (20 mL), dried over Na_2SO_4, and concentrated under reduced pressure. The residue could be used in the next steps without extra purification. Compound **4** was prepared in 75% yield as a colourless oil. ^{1}H NMR (300 MHz, $CDCl_3$) δ 7.79 (s, 1H), 7.68 (s, 1H), 4.07 (d, J = 7.5 Hz, 2H), 2.55−2.35 (m, 1H), 1.78−1.50 (m, 6H), 1.31 (s, 12H), 0.87−0.80 (m, 2H). ^{13}C NMR (75 MHz, $CDCl_3$) δ 144.63 (s), 136.14 (s), 83.32 (s), 56.77 (s), 40.56 (s), 30.21 (s), 24.90 (s), 24.75 (s).

4.1.3. Preparation of 3-chloro-4-(1-(cyclopentylmethyl)-1H-pyrazol-4-yl)benzonitrile (6a)

Compound **4** (2.2 mmol) was added to a solution of 5-bromo-6-chloropicolinonitrile (2.64 mmol), Pd(dppf)Cl_2 (0.44 mmol) and K_2CO_3 (5.5 mmol) in 1,4-dioxane (6 mL) and H_2O (2 mL). The mixture was stirred at ambient temperature for 10 min, and subsequently at 100 °C for 3 h. The reaction was cooled to ambient temperature and quenched with H_2O (15 mL). The mixture was extracted with ethyl acetate (3 × 20 mL). The combined organic layers were washed with H_2O (2 × 20 mL) brine (20 mL), dried over Na_2SO_4, and concentrated under reduced pressure. The residue was purified by chromatography on silica gel, elution being carried out with a mixture of ethyl acetate and hexane (1:3). Compound **6a** was prepared in 53% yield as a light-yellow solid. Melting point: 95−97 °C. ^{1}H NMR (300 MHz, $CDCl_3$) δ 8.01 (s, 1H), 7.93 (d, J = 7.9 Hz, 1H), 7.87 (s, 1H), 7.63 (d, J = 7.9 Hz, 1H), 4.11 (d, J = 7.5 Hz, 2H), 2.56−2.39 (m, 1H), 1.83−1.51 (m, 6H), 1.36−1.22 (m, 2H). ^{13}C NMR (75 MHz, $CDCl_3$) δ 148.94

(s), 138.83 (s), 137.30 (s), 132.81 (s), 129.84 (s), 129.57 (s), 127.26 (s), 116.14 (s), 115.83 (s), 57.58 (s), 40.63 (s), 30.25 (s), 24.96 (s).

4.1.4. Preparation of 2-chloro-3-(1-(cyclopentylmethyl)-1H-pyrazol-4-yl)-6-methylpyridine (**6b**)

Compound **6b** was prepared in a manner similar to that described for **6a** in 65% yield as a colorless oil. ^{1}H NMR (300 MHz, $CDCl_3$) δ 7.86 (s, 1H), 7.77 (s, 1H), 7.68 (d, J = 7.8 Hz, 1H), 7.10 (d, J = 7.8 Hz, 1H), 4.09 (d, J = 7.5 Hz, 2H), 2.58−2.39 (m, 4H), 1.82−1.53 (m, 6H), 1.37−1.21 (m, 2H). ^{13}C NMR (75 MHz, $CDCl_3$) δ 156.58 (s), 147.29 (s), 138.31 (s), 137.95 (s), 128.94 (s), 125.20 (s), 122.23 (s), 117.22 (s), 40.72 (s), 30.27 (s), 24.96 (s), 23.65 (s).

4.1.5. Preparation of 5-(1-(cyclopentylmethyl)-1H-pyrazol-4-yl)-6-(2-methyl-3-oxoisoindolin-5-yl)picolinonitrile (**8**)

A mixture of **6a** (0.4 mmol), 2-methyl-6-(4,4,5,5-tetramethyl-1,3,2-dioxaborolan-2-yl)isoindolin-1-one (0.48 mmol), Pd(dtbpf)Cl_2 (0.08 mmol) and K_2CO_3 (1.2 mmol) in 1,4-dioxane (1.5 mL) and H_2O (0.5 mL) was stirred at ambient temperature for 10 min, then 100 °C for 3 h. The reaction was cooled to ambient temperature and quenched with H_2O (10 mL). The mixture was extracted with ethyl acetate (3 × 15 mL). The combined organic layers were washed with H_2O (2 × 15 mL) and brine (15 mL), dried over Na_2SO_4, and concentrated under reduced pressure. The residue was purified by silica gel chromatography, elution being carried out with ethyl acetate. Compound **8** was prepared in 64% yield as a light-yellow solid. Melting point: 227−228 °C. ^{1}H NMR (300 MHz, $CDCl_3$) δ 7.88 (d, J = 7.7 Hz, 2H), 7.67 (d, J = 8.0 Hz, 1H), 7.59 (d, J = 7.7 Hz, 1H), 7.46 (d, J = 7.8 Hz, 1H), 7.29 (s, 1H), 6.96 (s, 1H), 4.41 (s, 2H), 3.88 (d, J = 7.5 Hz, 2H), 3.20 (s, 3H), 2.36−2.18 (m, 1H), 1.64−1.50 (m, 6H), 1.13−1.02 (m, 2H). ^{13}C NMR (75 MHz, $CDCl_3$) δ 167.76 (s), 157.72 (s), 141.46 (s), 139.32 (s), 138.29 (s), 137.21 (s), 133.30 (s), 132.16 (s), 131.38 (s), 130.82 (s), 128.81 (s), 127.24 (s), 124.45 (s), 122.89 (s), 117.95 (s), 117.26 (s), 57.22 (s), 51.88 (s), 40.50 (s), 30.09 (s), 29.50 (s), 24.85 (s).

4.1.6. Preparation of 4-(1-(cyclopentylmethyl)-1H-pyrazol-4-yl)-3-(3-oxoisoindolin-5-yl)benzonitrile (**9**)

Compound **9** was prepared in a manner similar to that described for **8** in 66% yield as a yellow solid. Melting point: 184−185 °C. ^{1}H NMR (300 MHz, $CDCl_3$) δ 7.86−7.95 (m, 2H), 7.72−7.63 (m, 2H), 7.54−7.46 (m, 2H), 7.33 (s, 1H), 6.97 (s, 1H), 4.51 (s, 2H), 3.90 (d, J = 7.5 Hz, 2H), 2.35−2.22 (m, 1H), 1.68−1.49 (m, 6H), 1.14−1.04 (m, 2H). ^{13}C NMR (75 MHz, $CDCl_3$) δ 171.00 (s), 157.58 (s), 144.09 (s), 139.32 (s), 138.27 (s), 137.34 (s), 132.84 (s), 132.47 (s), 131.34 (s), 130.92 (s), 128.82 (s), 127.27 (s), 124.71 (s), 123.48 (s), 117.94 (s), 117.24 (s), 57.21 (s), 45.62 (s), 40.53 (s), 30.08 (s), 24.86 (s).

4.1.7. Preparation of 6-(3-(1-(cyclopentylmethyl)-1H-pyrazol-4-yl)-6-methylpyridin-2-yl)-2-methylisoindolin-1-one (**10**)

Compound **10** was prepared in a manner similar to that described for **8** in 53% yield as a white solid. Melting point: 64−65 °C. ^{1}H NMR (300 MHz, $CDCl_3$) δ 7.90 (s, 1H), 7.63 (d, J = 7.9 Hz, 1H), 7.52 (dd, J = 7.8, 1.6 Hz, 1H), 7.36 (d, J = 7.8 Hz, 1H), 7.22 (s, 1H), 7.14 (d, J = 7.9 Hz, 1H), 6.85 (s, 1H), 4.36 (s, 2H), 3.84 (d, J = 7.5 Hz, 2H), 3.17 (s, 3H), 2.58 (s, 3H), 2.32−2.16 (m, 1H), 1.64−1.40 (m, 2H), 1.14−0.98 (m, 2H). ^{13}C NMR (75 MHz, $CDCl_3$) δ 168.22 (s), 156.27 (s), 155.47 (s), 141.39 (s), 140.37 (s), 138.14 (s), 137.31 (s), 133.01 (s), 132.45 (s), 128.14 (s), 124.68 (s), 124.30 (s), 122.30 (s), 122.22 (s), 119.39 (s), 56.95 (s), 51.83 (s), 40.60 (s), 30.06 (s), 29.43 (s), 24.85 (s), 24.23 (s).

4.1.8. Preparation of 6-(3-(1-(cyclopentylmethyl)-1H-pyrazol-4-yl)-6-methylpyridin-2-yl)isoindolin-1-one (**11**)

Compound **11** was prepared in a manner similar to that described for **8** in 26% yield as a white solid. Melting point: 55−56 °C. ^{1}H NMR (300 MHz, $CDCl_3$) δ 7.97 (s, 1H), 7.65 (d, J = 7.9 Hz, 1H), 7.60 (dd, J = 7.8, 1.5 Hz, 1H), 7.42 (d, J = 7.7 Hz, 2H), 7.27 (s, 1H), 7.17 (d, J = 7.9 Hz, 1H), 6.87 (s, 1H), 4.46 (s, 3H), 3.87 (d, J = 7.5 Hz, 3H), 2.60 (s, 3H), 2.38−2.18 (m, 1H), 1.70−1.45 (m, 6H), 1.20−0.99 (m, 2H). ^{13}C NMR (75 MHz, $CDCl_3$) δ 171.49 (s), 156.38 (s), 155.36 (s), 143.03 (s), 141.41 (s), 138.17 (s), 137.42 (s), 133.12 (s), 132.21 (s), 128.18 (s), 124.92 (s), 124.31 (s), 122.90 (s), 122.27 (s), 119.39 (s), 56.98 (s), 45.48 (s), 40.63 (s), 30.07 (s), 24.87 (s), 24.24 (s).

4.1.9. Preparation of 5-(1-(cyclopentylmethyl)-1H-pyrazol-4-yl)-6-(2-(2-fluoroethyl)-3-oxoisoindolin-5-yl)picolinonitrile (**12**)

A solution of **9** (0.13 mmol) in THF (1 mL) was added dropwise to a solution of NaH (0.37 mmol, 60% suspension) in THF (1 mL) at 0 °C. The mixture was stirred at ambient temperature for 1 h ICH_2CH_2F (0.26 mmol) was added and the resulting mixture was stirred at 60 °C for 4 h. The reaction was cooled to ambient temperature and quenched with H_2O (10 mL) at 0 °C. The mixture was extracted with ethyl acetate (3 × 15 mL). The combined organic layers were washed with H_2O (2 × 15 mL) brine (15 mL), dried over Na_2SO_4, and concentrated under reduced pressure. The residue was purified by chromatography on silica gel, elution being carried out with ethyl acetate. Compound **12** was prepared in 39% yield as a white solid. Melting point: 155−156 °C. ^{1}H NMR (300 MHz, $CDCl_3$) δ 7.93−7.85 (m, 2H), 7.68 (d, J = 8.0 Hz, 1H), 7.63 (dd, J = 7.8, 1.4 Hz, 1H), 7.48 (d, J = 7.8 Hz, 1H), 7.32 (s, 1H), 6.98 (s, 1H), 4.79−4.57 (m, 4H), 4.01−3.84 (m, 4H), 2.36−2.20 (m, 1H), 1.67−1.45 (m, 6H), 1.14−1.04 (m, 2H). ^{19}F NMR (282 MHz, $CDCl_3$) δ −216.87 (tt, J = 47.4, 28.8 Hz). ^{13}C NMR (75 MHz, $CDCl_3$) δ 167.83 (s), 157.60 (s), 142.08 (s), 139.38 (s), 138.28 (s), 137.28 (s), 132.67 (s), 132.56 (s), 131.33 (s), 130.90 (s), 128.78 (s), 127.25 (s), 124.65 (s), 122.99 (s), 117.94 (s), 117.24 (s), 83.30 (d, J = 168.8 Hz), 57.21 (s), 51.48 (s), 43.16 (d, J = 19.8 Hz), 40.50 (s), 30.07 (s), 24.86 (s).

4.1.10. Preparation of 5-(1-(cyclopentylmethyl)-1H-pyrazol-4-yl)-6-(2-(3-fluoropropyl)-3-oxoisoindolin-5-yl)picolinonitrile (**13**)

Compound **13** was prepared in a manner similar to that described for **12** in 37% yield as a white solid. Melting point: 188−189 °C. ^{1}H NMR (300 MHz, $CDCl_3$) δ 7.97−7.82 (m, 2H), 7.67 (d, J = 7.4 Hz, 1H), 7.60 (d, J = 7.2 Hz, 1H), 7.47 (d, J = 7.4 Hz, 1H), 7.28 (s, 1H), 7.01 (s, 1H), 4.65−4.43 (m, 4H), 3.93−3.72 (m, 4H), 2.41−2.24 (m, 1H), 2.21−2.01 (m, 2H), 1.65−1.50 (m, 6H), 1.15−1.03 (m, 2H). ^{19}F NMR (282 MHz, $CDCl_3$) δ −216.71 (tt, J = 47.1, 26.2 Hz). ^{13}C NMR (75 MHz, $CDCl_3$) δ 167.85 (s), 157.65 (s), 141.65 (s), 139.40 (s), 138.29 (s), 137.30 (s), 133.17 (s), 132.35 (s), 131.31 (s), 130.86 (s), 128.87 (s), 127.25 (s), 124.54 (s), 123.00 (s), 117.96 (s), 117.25 (s), 81.67 (d, J = 165.4 Hz), 57.23 (s), 50.38 (s), 40.49 (s), 39.28 (d, J = 5.3 Hz), 30.08 (s), 29.32 (d, J = 19.7 Hz), 24.88 (s).

4.2. Pharmacology

Materials: Chinese hamster ovary-FlpIn cells were obtained from Invitrogen, hygromycin B was purchased from Roche Applied Science (Indianapolis, IN). Dulbecco's modified Eagle's medium (DMEM) and fetal bovine serum (FBS) were purchased from Invitrogen (Carlsbad, CA) and ThermoTrace (Melbourne, Australia), respectively. [^{3}H]-*N*-methylscopolamine ([^{3}H]-NMS; 72 Ci/mmol) and [^{35}S]GTPγS (>1000 Ci/mmol) were purchased from PerkinElmer Life Sciences (Boston, MA). Acetylcholine was purchased from Sigma−Aldrich (St. Louis, MO). Cell Culture—FlpInCHO cells stably expressing the wild-type human muscarinic acetylcholine M_4 receptor (hM_4 mAChR) were grown in Dulbecco's modified Eagle's medium, supplemented with 5% fetal bovine serum (FBS), and were used directly for intact cell [^{3}H]-NMS binding assays, or expended to generate membranes preparations for [^{35}S]GTPγS binding assays. Membrane preparations—cells were grown until approximately 90% confluence and harvested using 2 nmol/L EDTA in phosphate-buffered saline (137 nmol/L NaCl, 2.7 nmol/L KCl, 4.3 nmol/L Na_2HPO_4, and 1.5 nmol/L KH_2PO_4; PBS). Cells were pelleted by centrifugation at 1200×*g* for 10 min, and the pellets were resuspended in 30 mL of buffer containing 20 nmol/L HEPES and 10 nmol/L EDTA at pH 7.4. All subsequent steps were performed at 4 °C. The cell suspension was homogenized using a Polytron homogenizer (PT 1200 CL; Kinematica, Basel, Switzerland), with two 10 s bursts separated by cooling on ice for a minimum of 30 s. The cell homogenate was centrifuged at 1700×*g* for 5 min, and the supernatant was transferred to new tubes and further centrifuged (38,000×*g*, 90 min) in a Sorval centrifuge. The pellet was resuspended in 10 mL of buffer (20 nmol/L HEPES and 0.1 nmol/L EDTA, pH 7.4) and briefly homogenized to ensure uniform consistency. The protein concentration was determined by the method of Bradford using bovine serum albumin as a standard.

Whole cell radioligand binding assays: FlpIn CHO cells stably expressing the hM_4 were plated at the density of 20,000 per well of 96-well white clear bottom Isoplates (PerkinElmer Life Sciences, Boston, MA), and grown overnight at 37 °C. The following day, cells were washed twice with PBS, and incubated with increasing concentrations of ACh in the presence or absence of increasing concentrations of M_4-PAMs, and [^{3}H]-NMS (∼0.1 nmol/L) in a final volume of 200 µL. Atropine at the final concentration of 10 µmol/L was used to determine non-specific binding. The assays were terminated by rapid removal of the radioligand, and two washes with 100 µL/well of ice-cold 0.9% NaCl buffer. Radioactivity was determined by addition of 100 µL/well MicroScint scintillation liquid (PerkinElmer Life Sciences, Boston, MA), and counting in a MicroBeta plate reader (PerkinElmer Life Sciences, Boston, MA).

[^{35}S]-GTPγS Binding Assay: Membrane homogenates (15 µg) were equilibrated in a 500 µL total volume of assay buffer containing 10 µmol/L guanosine 5′-diphosphate and a range of concentrations of ACh (10 nmol/L−10 mmol/L in the absence or presence of M_4-PAMs (0.1−10 µmol/L) at 30 °C for 60 min. After this time, 50 µL of [^{35}S]-GTPγS (1 nmol/L) was added, and incubation continued for 30 min at 30 °C. Incubation was terminated by rapid filtration through Whatman GF/B filters using a Brandell cell harvester (Gaithersburg, MD). Filters were washed three times with 3 mL aliquots of ice-cold 0.9% NaCl buffer and dried before the addition of 4 mL of Ultima Gold (PerkinElmer Life Sciences, Boston, MA). Vials were then left to stand until the filters became uniformly translucent before radioactivity was determined in cpm using scintillation counting.

All computerized nonlinear regression was performed using the program Prism 9.01 (GraphPad Software, San Diego, CA, USA). Binding interaction studies between ACh and M_4-PAMs were fitted to the following allosteric ternary complex model Eq. (1):

$$Y = \frac{B_{\max}[D]}{[D] + \left(\frac{K_D K_B}{\alpha'[B] + K_B}\right)\left(1 + \frac{[I]}{K_I} + \frac{[B]}{K_B} + \frac{\alpha[I][B]}{K_I K_B}\right)} \quad (1)$$

where B_{max} is the total number of receptors, [*D*], [*B*] and [*I*] denote the concentrations of radioligand, allosteric ligand, and orthosteric ligand, respectively, and K_D, K_B and K_I represent their respective equilibrium dissociation constants. α' and α are the cooperativity factors between the M_4-PAMs and radioligand or ACh, respectively. Values of α or α' greater than 1 denote positive cooperativity, values between 0 and 1 denote negative cooperativity, and a value of 1 indicates neutral cooperativity.

Functional interaction studies between ACh and M_4-PAMs in [^{35}S]-GTPγS binding assays were analyzed using the following operational model of allosterism and agonism Eq. (2):

$$E = \text{Basal} + \frac{(E_{\max} - \text{Basal})([A](K_B + \alpha\beta + \tau_B[B][EC_{50}])^n}{[EC_{50}]^n(K_B + [B])^n + ([A](K_B + \alpha\beta[B]) + \tau_B[B][EC_{50}])^n} \quad (2)$$

where E_{max} is the maximal possible system response, and Basal is the response in the absence of agonist. K_B is the equilibrium dissociation constant of allosteric ligand, and EC_{50} is the concentration of orthosteric agonist required to achieve half maximal response. [*A*] and [*B*] denote concentrations of orthosteric and allosteric ligands, respectively. α and β denote allosteric effects on orthosteric ligand binding affinity and efficacy, respectively, and τ_B denotes the efficacy of allosteric ligand.

Tango assays were performed as previously reported[47]. Briefly, HEK293 cells stably, expressing a tTA-dependent luciferase reporter and a β-arrestin2-TEV fusion gene, were maintained in DMEM supplemented with 10% FBS, 2 µg/mL puromycin, 100 µg/mL hygromycin B 100 U/mL penicillin and 100 µg/mL streptomycin in a humidified atmosphere at 37 °C in 5% carbon dioxide. Cells were then plated at 9 × 106 to 10 × 106 cells per 150-mm cell-culture dish for transfection. The following day, cells were transfected and on Day 3, the transfected cells were transferred in 50 µL of medium at 15,000 to 20,000 cells per well into poly-L-lysine-coated cell-culture plates. On Day 4, test ligand solutions were prepared in filter-sterilized assay buffer, consisting of 20 nmol/L HEPES and 1 × HBSS, pH 7.4, and 20 µL was added to each well. On Day 5, medium and drug solutions were removed from the wells, whereas 20 µL per well of Bright-Glo solution (Promega) diluted 20-fold in assay buffer was added to each well. Following an incubation period of 15−20 min at room temperature, luminescence was measured in a Trilux luminescence counter. Results are presented as luminescence units (RLU).

4.3. Radiochemistry

[^{18}F]Fluoride ions were generated in a cyclotron (18 MeV protons and >98% enriched $H_2^{18}O$) *via* the nuclear reaction of $^{18}O(p, n)^{18}F$. [^{18}F]fluoride ions were purified using an anion-exchange cartridge (Sep-Pak QMA Plus Light cartridge; Waters Cat. No.

186004540), whereas the elution from the cartridge was conducted with a solution of TBAOMs (3 mg) in MeOH (1 mL). After evaporation of the MeOH at 110 °C with a helium flow (10 min), a solution of tosylate precursor **14** (3 mg) in dry-MeCN/*t*BuOH (50/350 μL) was added, and the reaction mixture was left at 100 °C for 10 min. After cooling to ambient temperature, water (10 mL) was added and the resulting mixture passed through a Sep-Pak light C18 (Waters Cat. No. WAT023501). The product was eluted with acetonitrile (1 mL) and, following the addition of 2 mL water, purified by HPLC (Waters XSelect HSS T3 OBD™ Prep Column, 5 μm, 10 mm × 250 mm) with a flow rate of 5 mL/min using a mixture of acetonitrile/H_2O (*v*/*v* = 45/55, containing 0.1% NEt_3). The UV signal was monitored at a wavelength of 254 nm and the radioactive [^{18}F]**12** fraction was collected. After dilution with water (10 mL), the product was loaded onto an activated Sep-Pak light C18 (Waters cat. No. WAT023501), washed with 10 mL of water, and eluted with ethanol (0.5 mL). The final product was formulated in saline (5% ethanol). Chemical and radiochemical purity were assessed by analytical HPLC (XBridge, C18 column, 5 μm, 4.6 mm × 100 mm) with an eluent of CH_3CN/H_2O (45/55, *v*/*v*) at a flow rate of 1.0 mL/min.

4.4. *In vitro autoradiography*

In vitro autoradiography was performed as previously reported by our group[48], however, with minor modifications. Briefly, mouse, rat, NHP and human brain tissues were cryosectioned into 20 μm sections and stored at −80 °C until the day of experiment. Cryosections were preincubated in the assay buffer (50 nmol/L Tris, pH 7.4) for 10 min at ambient temperature. Following the addition of [^{18}F]**12**, sections were incubated at ambient temperature for 40 min. For blocking studies, non-radioactive **11** was added to the assay buffer. After incubation, brain sections were dipped in distilled water (3 × 5 s). All experiments were conducted in the presence and in the absence of carbachol. Brain sections were dried on air and subsequently exposed imaging plates (BASMS2025, GE Healthcare, NJ, USA) for 120 min. For quantification, ROIs were manually drawn on the autoradiograms. The radioactivity was measured on a Bio-Imaging analyzer system (BAS5000, Fujifilm) and normalized to a reference region.

4.5. *PET/MRI imaging*

Two male rhesus monkeys (weight range 4.1−4.5 kg) underwent PET scanning for 60 min with the head centered in the field of view. The tracer solution containing [^{18}F]**12** (5.928−5.994 mCi, 0.36−0.77 μg) in saline were injected to the monkey *via* a flexible percutaneous venous catheter. MRI was used for anatomical orientation. PET images were reconstructed and analyzed with PMOD (Zurich, Switzerland). Volumes of interest were defined based on the brain region assignment by MRI. Decay-corrected radioactivity is expressed as standardized uptake values (SUVs, radioactivity per mL tissue)/(injected radioactivity) × body weight.

Acknowledgments

We thank Allan I. Levey for reviewing the manuscript. AH was supported by the Swiss National Science Foundation (SNSF). This work was supported by the National Health and Medical Research Council (NHMRC) Program Grant (APP1055134, USA) and the Australian Research Council (ARC) Discovery Project (DP190102950, USA). TEJ was supported by grants from Fulbright Denmark, The Lundbeck Foundation, Eva and Henry Frænkels foundation, The Danish Cancer Society, The Harboe Foundation, Dr. Phil Ragna Rask-Nielsens Grundforskningsfond, Kong Christian den Tiendes fond, Carl og Ellen Hertz' legat, The Scandinavian Society of Clinical Physiology and Nuclear Medicine, Christian og Otilla Brorsons Rejselegat, A.P. Møller fonden and Helsefonden.

Author contributions

Study conceptualization: Ahmed Haider, Celine Valant, Steven H. Liang; probe development and characterization: Ahmed Haider, Xiaoyun Deng, Olivia Mastromihalis, Stefanie K. Pfister, Troels E. Jeppesen, Zhiwei Xiao, Vi Pham, Shaofa Sun, Jian Rong, Chunyu Zhao, Jiahui Chen, Yinlong Li; data acquisition, analyses, and quality control: Ahmed Haider, Xiaoyun Deng, Olivia Mastromihalis, Stefanie K. Pfister, Troels E. Jeppesen, Zhiwei Xiao, Vi Pham, Shaofa Sun, Jian Rong, Chunyu Zhao, Jiahui Chen, Yinlong Li, Theresa R. Connors, April T. Davenport, James B. Daunais, Vahid Hosseini, Wenqing Ran, Arthur Christopoulos, Lu Wang; Manuscript drafting, editing and reviewing: Ahmed Haider, Celine Valant, Steven H. Liang.

Conflicts of interest

The authors declare no conflict of interest.

Appendix A. Supporting information

Supporting data to this article can be found online at https://doi.org/10.1016/j.apsb.2022.07.008.

References

1. Caulfield MP, Birdsall NJ. International Union of Pharmacology. XVII. Classification of muscarinic acetylcholine receptors. *Pharmacol Rev* 1998;**50**:279−90.
2. Caulfield MP. Muscarinic receptors—characterization, coupling and function. *Pharmacol Ther* 1993;**58**:319−79.
3. Lebois EP, Thorn C, Edgerton JR, Popiolek M, Xi S. Muscarinic receptor subtype distribution in the central nervous system and relevance to aging and Alzheimer's disease. *Neuropharmacology* 2018;**136**:362−73.
4. Kruse AC, Kobilka BK, Gautam D, Sexton PM, Christopoulos A, Wess J. Muscarinic acetylcholine receptors: novel opportunities for drug development. *Nat Rev Drug Discov* 2014;**13**:549−60.
5. Hulme EC, Birdsall NJ, Buckley NJ. Muscarinic receptor subtypes. *Annu Rev Pharmacol Toxicol* 1990;**30**:633−73.
6. Lanzafame AA, Christopoulos A, Mitchelson F. Cellular signaling mechanisms for muscarinic acetylcholine receptors. *Recept Channel* 2003;**9**:241−60.
7. He N, Mao LM, Sturich AW, Jin DZ, Wang JQ. Inhibition of basal and amphetamine-stimulated extracellular signal-regulated kinase (ERK) phosphorylation in the rat forebrain by muscarinic acetylcholine M4 receptors. *Brain Res* 2018;**1688**:103−12.
8. Mulugeta E, Karlsson E, Islam A, Kalaria R, Mangat H, Winblad B, et al. Loss of muscarinic M4 receptors in hippocampus of Alzheimer patients. *Brain Res* 2003;**960**:259−62.
9. Ahmed T, Zahid S, Mahboob A, Farhat SM. Cholinergic system and post-translational modifications: an insight on the role in Alzheimer's disease. *Curr Neuropharmacol* 2017;**15**:480−94.

10. Raedler TJ, Bymaster FP, Tandon R, Copolov D, Dean B. Towards a muscarinic hypothesis of schizophrenia. *Mol Psychiatr* 2007;**12**:232−46.
11. Crook JM, Dean B, Pavey G, Copolov D. The binding of [3H]AF-DX 384 is reduced in the caudate-putamen of subjects with schizophrenia. *Life Sci* 1999;**64**:1761−71.
12. Colloby SJ, Nathan PJ, McKeith IG, Bakker G, O'Brien JT, Taylor JP. Cholinergic muscarinic M1/M4 receptor networks in dementia with Lewy bodies. *Brain Commun* 2020;**2**:fcaa098.
13. de la Cour C, Sørensen G, Wortwein G, Weikop P, Dencker D, Fink-Jensen A, et al. Enhanced self-administration of alcohol in muscarinic acetylcholine M4 receptor knockout mice. *Eur J Pharmacol* 2015;**746**:1−5.
14. Schmidt LS, Thomsen M, Weikop P, Dencker D, Wess J, Woldbye DPD, et al. Increased cocaine self-administration in M4 muscarinic acetylcholine receptor knockout mice. *Psychopharmacol* 2011;**216**:367−78.
15. Wang Y, Li W, Lohith TG, Bormans G, Koole M, Van Laere K, et al. IC-P-150: [C-11]MK-6884 PET: characterizing brain M4 receptors in healthy elderly volunteers and acetylcholinesterase inhibitors-treated AD patients. *Alzheimers Dement* 2019;**15**:P121.
16. Volpicelli LA, Levey AI. Muscarinic acetylcholine receptor subtypes in cerebral cortex and hippocampus. *Prog Brain Res* 2004;**145**:59−66.
17. Eglen RM. Muscarinic receptor subtypes in neuronal and non-neuronal cholinergic function. *Auton Autacoid Pharmacol* 2006;**26**:219−33.
18. Levey AI. Muscarinic acetylcholine receptor expression in memory circuits: implications for treatment of Alzheimer disease. *Proc Natl Acad Sci U S A* 1996;**93**:13541−6.
19. Odagaki Y, Kinoshita M, Toyoshima R. Functional activation of G-proteins coupled with muscarinic acetylcholine receptors in rat brain membranes. *J Pharmacol Sci* 2014;**125**:157−68.
20. Radu BM, Osculati AMM, Suku E, Banciu A, Tsenov G, Merigo F, et al. All muscarinic acetylcholine receptors (M1-M5) are expressed in murine brain microvascular endothelium. *Sci Rep* 2017;**7**:5083.
21. Bernard V, Levey AI, Bloch B. Regulation of the subcellular distribution of m4 muscarinic acetylcholine receptors in striatal neurons *in vivo* by the cholinergic environment: evidence for regulation of cell surface receptors by endogenous and exogenous stimulation. *J Neurosci* 1999;**19**:10237−49.
22. Suratman S, Leach K, Sexton PM, Felder CC, Loiacono RE, Christopoulos A. Impact of species variability and 'probe-dependence' on the detection and *in vivo* validation of allosteric modulation at the M4 muscarinic acetylcholine receptor. *Br J Pharmacol* 2011;**162**:1659−70.
23. Shannon HE, Bymaster FP, Calligaro DO, Greenwood B, Mitch CH, Sawyer BD, et al. Xanomeline: a novel muscarinic receptor agonist with functional selectivity for M1 receptors. *J Parmacol Exp Ther* 1994;**269**:271−81.
24. Shekhar A, Potter WZ, Lightfoot J, Lienemann J, Dubé S, Mallinckrodt C, et al. Selective muscarinic receptor agonist xanomeline as a novel treatment approach for schizophrenia. *Am J Psychiatr* 2008;**165**:1033−9.
25. Bodick NC, Offen WW, Levey AI, Cutler NR, Gauthier SG, Satlin A, et al. Effects of xanomeline, a selective muscarinic receptor agonist, on cognitive function and behavioral symptoms in Alzheimer disease. *Arch Neurol* 1997;**54**:465−73.
26. Burger WAC, Sexton PM, Christopoulos A, Thal DM. Toward an understanding of the structural basis of allostery in muscarinic acetylcholine receptors. *J Gen Physiol* 2018;**150**:1360−72.
27. Chan WY, McKinzie DL, Bose S, Mitchell SN, Witkin JM, Thompson RC, et al. Allosteric modulation of the muscarinic M4 receptor as an approach to treating schizophrenia. *Proc Natl Acad Sci U S A* 2008;**105**:10978−83.
28. Leach K, Loiacono RE, Felder CC, McKinzie DL, Mogg A, Shaw DB, et al. Molecular mechanisms of action and *in vivo* validation of an M4 muscarinic acetylcholine receptor allosteric modulator with potential antipsychotic properties. *Neuropsychopharmacology* 2010;**35**:855−69.
29. Shirey JK, Xiang Z, Orton D, Brady AE, Johnson KA, Williams R, et al. An allosteric potentiator of M4 mAChR modulates hippocampal synaptic transmission. *Nat Chem Biol* 2008;**4**:42−50.
30. Brady AE, Jones CK, Bridges TM, Kennedy JP, Thompson AD, Ju Heiman, et al. Centrally active allosteric potentiators of the M4 muscarinic acetylcholine receptor reverse amphetamine-induced hyperlocomotor activity in rats. *J Pharmacol Exp Therapeut* 2008;**327**:941−53.
31. Conn PJ, Jones CK, Lindsley CW. Subtype-selective allosteric modulators of muscarinic receptors for the treatment of CNS disorders. *Trends Pharmacol Sci* 2009;**30**:148−55.
32. Kennedy JP, Bridges TM, Gentry PR, Brogan JT, Kane AS, Jones CK, et al. Synthesis and structure−activity relationships of allosteric potentiators of the M4 muscarinic acetylcholine receptor. *ChemMedChem* 2009;**4**:1600−7.
33. Conn PJ, Lindsley CW, Meiler J, Niswender CM. Opportunities and challenges in the discovery of allosteric modulators of GPCRs for treating CNS disorders. *Nat Rev Drug Discov* 2014;**13**:692−708.
34. Wood MR, Noetzel MJ, Poslusney MS, Melancon BJ, Tarr JC, Lamsal A, et al. Challenges in the development of an M 4 PAM *in vivo* tool compound: the discovery of VU0467154 and unexpected DMPK profiles of close analogs. *Bioorg Med Chem Lett* 2017;**27**:171−5.
35. Bubser M, Bridges TM, Dencker D, Gould RW, Grannan M, Noetzel MJ, et al. Selective activation of M4 muscarinic acetylcholine receptors reverses MK-801-induced behavioral impairments and enhances associative learning in rodents. *ACS Chem Neurosci* 2014;**5**:920−42.
36. Salovich JM, Vinson PN, Sheffler DJ, Lamsal A, Utley TJ, Blobaum AL, et al. Discovery of *N*-(4-methoxy-7-methylbenzo[*d*]thiazol-2-yl)isonicatinamide, ML293, as a novel, selective and brain penetrant positive allosteric modulator of the muscarinic 4 (M4) receptor. *Bioorg Med Chem Lett* 2012;**22**:5084−8.
37. Tarr JC, Wood MR, Noetzel MJ, Bertron JL, Weiner RL, Rodriguez AL, et al. Challenges in the development of an M4 PAM preclinical candidate: the discovery, SAR, and *in vivo* characterization of a series of 3-aminoazetidine-derived amides. *Bioorg Med Chem Lett* 2017;**27**:2990−5.
38. Le U, Melancon BJ, Bridges TM, Vinson PN, Utley TJ, Lamsal A, et al. Discovery of a selective M4 positive allosteric modulator based on the 3-amino-thieno[2,3-*b*]pyridine-2-carboxamide scaffold: development of ML253, a potent and brain penetrant compound that is active in a preclinical model of schizophrenia. *Bioorg Med Chem Lett* 2013;**23**:346−50.
39. Spock M, Carter TR, Bollinger KA, Han C, Baker LA, Rodriguez AL, et al. Discovery of VU6028418: a highly selective and orally bioavailable M4muscarinic acetylcholine receptor antagonist. *ACS Med Chem Lett* 2021;**12**:1342−9.
40. Wood MR, Noetzel MJ, Melancon BJ, Poslusney MS, Nance KD, Hurtado MA, et al. Discovery of VU0467485/AZ13713945: an M4 PAM evaluated as a preclinical candidate for the treatment of schizophrenia. *ACS Med Chem Lett* 2017;**8**:233−8.
41. Deng X, Hatori A, Chen Z, Kumata K, Shao T, Zhang X, et al. Synthesis and preliminary evaluation of 11C-labeled VU0467485/AZ13713945 and its analogues for imaging muscarinic acetylcholine receptor subtype 4. *ChemMedChem* 2019;**14**:303−9.
42. Deng X, Zhang Y, Rong J, Kumata K, Shao T, Wang G, et al. Synthesis and preliminary evaluation of 18F-labeled 1-(6,7-dimethyl-4-(methylamino)-1,3-dihydro-2*H*-pyrrolo[3,4-*c*]pyridin-2-yl)-2-(*trans*-2-(6-fluoropyridin-3-yl)cyclopropyl)ethan-1-one for imaging muscarinic acetylcholine receptor subtype 4. *Tetrahedron Lett* 2020;**61**:152060.
43. Tong L, Li W, Lo MMC, Gao X, Wai JMC, Rudd M, et al. Discovery of [11C]MK-6884: a positron emission tomography (PET) imaging agent for the study of M4muscarinic receptor positive allosteric modulators (PAMs) in neurodegenerative diseases. *J Med Chem* 2020;**63**:2411−25.
44. Deng X, Chen Z, Zhang X, Shao T, Shao Y, Liang S. Novel ^{11}C-labeled positive allosteric modulators for imaging muscarinic acetylcholine receptor M_4. *J Nucl Med* 2018;**59**(suppl 1):1023.

45. Acton JJ, III, Bao J, Egbertson M, Gao X, Harrison ST, Knowles SL, et al, inventors. Merck Sharp & Dorhm Corp., MSD R&D (China) Co., Ltd., assignees. 3-(1*H*-Pyrazol-4-yl) pyridine allosteric modulators of the M4 muscarinic acetylcholine receptor. PCT/CN2017/090384, 2017 June 27.
46. Li W, Wang Y, Lohith TG, Zeng Z, Tong L, Mazzola R, et al. The PET tracer [^{11}C]MK-6884 quantifies M4 muscarinic receptor in rhesus monkeys and patients with Alzheimer's disease. *Sci Transl Med* 2022; **14**:eabg3684.
47. Kroeze WK, Sassano MF, Huang XP, Lansu K, McCorvy JD, Giguère PM, et al. PRESTO-Tango as an open-source resource for interrogation of the druggable human GPCRome. *Nat Struct Mol Biol* 2015;**22**:362–9.
48. Haider A, Xiao Z, Xia X, Chen J, Van RS, Kuang S, et al. Development of a triazolobenzodiazepine-based PET probe for subtype-selective vasopressin 1A receptor imaging. *Pharmacol Res* 2021; **173**:105886.